REGULAR ARTICLE

Barium strontium titanate-based perovskite materials from DFT perspective: assessing the structural, electronic, vibrational, dielectric and energetic properties

Weber Duarte Mesquita[1] · Sabrina Rodrigues de Jesus[2] · Marisa Carvalho Oliveira[3] · Renan A. Pontes Ribeiro[4] ·
Maria Rita de Cássia Santos[2] · Mario Godinho Junior[2] · Elson Longo[5] · Maria Fernanda do Carmo Gurgel[2]

Abstract

This paper presents a current theoretical study on structural, electronic, vibrational, dielectric and energetic properties of the pristine cubic and tetragonal barium strontium titanate (BST_c and BST_t), as well as Sn-doped cubic and tetragonal barium strontium titanate ($BSTS_c$ and $BSTS_t$) crystals. For this purpose, first-principle calculations within the Density Functional Theory method at the B3LYP level are implemented in the CRYSTAL14 code. Structural and thermodynamic analysis indicates that the change in geometry, as well as the Sn-doping process in BST samples, induces structural defects, which govern its electronic structure, generating singular bandgap values attributed to the perturbation of electronic levels in the vicinity of the Fermi level. Moreover, the vibration analysis was helpful to identify how the Sr and Sn doping process along with the A- and B-site of perovskite structure can affect the structural disorder, mainly for the tetragonal phase. Besides, electron density maps showed that the electronic properties were associated with the presence of $[AO_{12}]$ (A=Ba and Sr) and $[MO_6]$ (M=Ti and Sn) clusters with distinct bonding character. Furthermore, our structural, vibrational, and electronic calculations are in good agreement with the available experimental data and pave the avenue towards the complete understanding of the overall properties of perovskite materials.

Keywords Density functional theory · Perovskite · Barium strontium titanate (BST) · Sn-doped BST structure · Electronic Structure · Disorder

1 Introduction

Perovskite oxides with general formula ABO_3 have attracted much attention due to their excellent physical and chemical properties across a wide range of technological fields, including electronics, optics, optoelectronics, etc. Different A-site and B-site dopants (where A=Sr, Ba; B=Ti, Sn) are used to modify the electrical properties of perovskite [1–12]. A solid solution of both $BaTiO_3$ and $SrTiO_3$ produces the barium strontium titanate ($Ba_xSr_{1-x}TiO_3$, BST) [3, 13–15], or as mentioned by Yustanti et al. [16] and Pasha et al. [17] with the presence of Sr ions as a dopant in $BaTiO_3$ formed BST crystal structure. BST is a promising material, due to its dielectric properties, adjusting the mole ratio of Ba/Sr to meet a wide variety of applications in electronics, such as microwave phase shifters, dielectric capacitors, dynamic random-access memories (DRAM), etc. Various preparation methods for BST have been investigated, as conventional

✉ Marisa Carvalho Oliveira
   marisa-coliveira@hotmail.com

1   Institute of Physics, Federal University of Catalão, Av. Dr.
    Lamartine Pinto de Avelar, Catalão, GO 75704-020, Brazil

2   Institute of Chemistry, Federal University of Catalão,
    Av. Dr. Lamartine Pinto de Avelar, Catalão, GO 75704-020,
    Brazil

3   LSQM – Laboratory of Chemical Synthesis of Materials,
    Department of Materials Engineering, Federal University
    of Rio Grande do Norte – UFRN, P.O. Box 1524, Natal, RN,
    Brazil

4   Department of Chemistry, State University of Minas Gerais,
    Av. Paraná, 3001, Divinópolis, MG 35501-170, Brazil

5   CDMF- Functional Materials Development Center,
    Federal University of São Carlos - UFSCar, P.O. Box 676,
    São Carlos, SP, Brazil

solid-state reaction [15, 18–20], solvothermal [21], sol–gel [22, 23], coprecipitation [24], spray pyrolysis[25], organic precursor method [26] and hydrothermal methods [13, 27].

The pure compounds, $BaTiO_3$ and $SrTiO_3$, have the same cubic perovskite structure in the high-temperature phase. Barium titanate is a typical ferroelectric, which undergoes three consecutive phase transitions from a cubic Pm3m to a tetragonal P4mm phase at 403 K, then to an orthorhombic Amm2 phase at 278 K, and, finally, to a rhombohedral R3m phase at 183 K. Studies on the $Ba_xSr_{1-x}TiO_3$ report the dependence of the temperatures of such phase transitions versus Sr content (x) [16, 18, 28, 29].

The ideal perovskite has a cubic space group *Pm-3 m* that contains one unit formula per cell. In particular, the A-site cation is 12-fold coordinated, while the B-site cation is coordinated by six O anions in a body-face-centered cubic structure[30]. Furthermore, most of the perovskite materials can present a slightly distorted structure obtained from the cubic structure by different ways, such as the displacement of ions from the ideal position, tilting the BO_6 octahedral, or defects in the structure that can break the cubic symmetry resulting in a "non-cubic" structure [10, 31].

Theoretical studies of perovskite compounds are of particular significance because they can be performed by different methods helping to explain the experimental results [32]. However, if a dopant is introduced in the compound, its properties are changed, and the ab initio simulations become far more complicated. In this case, the doping of titanate-based perovskites with several kinds of metals cations is widely performed because of the vast range of peculiar properties it allows to tune in fields as diverse as structural, electrical, and optical properties [33–35].

In this study, DFT calculations were applied to rationalize the effects of local structural changes induced by the introduction of Sn^{4+} in the crystal lattice and on the change in geometry of BST structure. We also demonstrate that the electronic properties are associated with the presence of different clusters with a unique bonding environment from electron density distribution. In particular, the formation of intermediate levels in the bandgap (E_{gap}) region was discussed following the structural disorders. Also, the thermodynamic stability of the pristine BST (cubic and tetragonal; BST_c and BST_t) and Sn-doped ($BSTS_c$ and $BSTS_t$) structures were analyzed to discuss the primary role of doping on the geometry stabilization. Notably, our models support the available experimental results, showing an excellent agreement. The manuscript is organized into three other sections in the following manner: (i) the next Sect. (2) describes in details the employed computational methodologies; (ii) Sect. 3 contains the results for structural, electronic, vibrational, and energetic properties; (iii) at last, the Sect. 4 contains the main conclusions of our work.

2 Computational details

The computational methods and theoretical procedures have been employed to study the bulk related to pristine cubic and tetragonal BST, as well as Sn-doped BST models with a doping amount of 50%, respectively. Calculations were carried out using the periodic ab initio CRYSTAL14 package [36] based on Density Functional Theory (DFT) using hybrid functional B3LYP [37, 38]. This computational technique has been successfully applied for the study of the electronic and structural properties of various materials, including perovskite and several other oxides[39–49]. In all calculations, the atomic centers were described by standard all-electron basis set 6–31G*, 976–41(*d*51)G, 9763–311(*d*631)G, 86–411(d31) G, and 9,763,111,631 for the O, Sr, Ba, Ti, and Sn atoms, respectively[40, 41, 50, 51].

Further, the electronic properties were analyzed in terms of the Density of States (DOS), Band Structure profiles, and the charge density map. Besides, Visualization for Electronic and Structural Analysis (VESTA) [52] and X-Window Crystalline Structures and Densities (XCrySDen) [53] software were used for visualization and representation of supercell models, X-ray diffraction (XRD) pattern calculation and the charge density maps construction. Electronic integration was performed using a dense $8\times8\times8$ Monkhorst–Pack [54] *k*-mesh for the pristine and doped cells, containing 75 k-points for both BST (cubic and tetragonal) and Sn-doped BST models. The accuracy of the Coulomb and exchange integral calculations were controlled by five thresholds set to 8, 8, 8, 8, and 16. The converge criterion for mono- and bi-electronic integrals were set to 10^{-8} Ha, while the root-mean-square (RMS) gradient, RMS displacement, maximum gradient, and maximum displacement were set to 9.4×10^{-5}, 7.3×10^{-4}, 1.4×10^{-4}, and 1.2×10^{-3} a.u. for BST_c, 1.9×10^{-4}, 8.3×10^{-4}, 3.4×10^{-4}, and 1.7×10^{-3} a.u. for $BSTS_c$, and 6.1×10^{-5}, 4.7×10^{-4}, 1.3×10^{-4}, and 8.2×10^{-4} a.u., for BST_t respectively. In all cases, both lattice parameters and atomic positions were relaxed.

In this work, a cubic and tetragonal supercell model of 10 atoms, which corresponds to a $1\times1\times2$ conventional cell, was used to simulate both pristine and Sn-doped BST structures. In particular, for the Sn-doped BST model, a $1\times1\times2$ supercell (10 atoms) was considered, where one Ti^{4+} (ionic radius 0.605 Å) cations were replaced by Sn^{4+} (ionic radius 0.690 Å) [55] corresponding to a doping concentration of 50%.

3 Results and discussion

3.1 Structural properties

The initial lattice parameters and atomic position used in the optimization process were obtained from the BST_c,

BST_t, $BSTS_c$, and $BSTS_t$, results of the Rietveld refinement, according to Souza et al. [56] and Chihaoui et al. [57]. The calculated values for the pristine barium strontium titanate $(Ba,Sr)TiO_3$ (BST) (cubic and tetragonal; BST_c and BST_t) and Sn-doped ($BSTS_c$ and $BSTS_t$) structures are collected in Table 1 and compared with experimental results.

As can be observed in Table 1, the crystal structure and the lattice parameters of theoretical results exhibit a small mean percentage error in comparison with the experimental results, evidencing that our calculations are in agreement with the experiments. Moreover, the unit-cell volume was underestimated by 1.41% and 3.01% for pristine BST_c, and BST_t, while the obtained results for $BSTS_c$ and $BSTS_t$ indicate an overestimation of 2.88% and 1.83%, respectively. Furthermore, comparing the crystalline parameters for both pristine and Sn-doped BST models, it was observed that for cubic polymorphs (BST_c and $BSTS_c$) an expansion of cell parameters of ~2.13% was found after the Sn doping, as well as for BST_t and $BSTS_t$ models with a variation of 5.52%. This behavior can be explained by the differences between the ionic radius of Sn^{4+} (0.690 Å) and Ti^{4+} ions (0.605 Å).

From a theoretical point of view, three models were constructed using a conventional $1 \times 1 \times 2$ supercell containing 10 atoms. First, structural and electronic properties were calculated for a perfect bulk of BST_c, and BST_t lattice, and $BSTS_c$, posteriorly. The representation of the BST_c, BST_t, and $BSTS_c$ bulk structures is shown in Fig. 1. This Fig. 1(a-c) illustrates the green, blue, gray, and red balls correspond to Ba, Sr, Ti, Sn, and O atoms, respectively. In this case, the Ti and Sn atoms are coordinated by six O atoms, producing octahedral $[TiO_6]$ and $[SnO_6]$ clusters. Correspondingly, the Ba and Sr atoms are coordinated to twelve O atoms, resulting in $[BaO_{12}]$ and $[SrO_{12}]$ clusters.

Furthermore, in order to analyze the structural disorder caused by the change in geometry, as well as the role of the Sn-doping in BST matrix, the bonding environment of both $[TiO_6]$, $[SnO_6]$, $[BaO_{12}]$ and $[SrO_{12}]$ clusters was

investigated in details. Table S1 (Supplementary Information) shows the calculated B3LYP values of bond distances (M–O) and the atomic coordinates in Cartesian coordinates (Å) along the $1 \times 1 \times 2$ supercell used for $BSTS_c$, BST_c, $BSTS_c$, BST_t, and $BSTS_t$, respectively.

It is important to note that atomic coordinates and M–O bond distances are stretched and shortened in the cubic, tetragonal and doped structures, respectively (see Table S1). This effect can be related to the structural order–disorder effect associated with the change in geometry and the insertion of the Sn dopant. Besides, the bond distances (M–O) undergo a slight increase in comparing Sn^{4+} and Ti^{4+} centers. The increase in bond distances (M–O) can be due to three reasons: (i) the distortion of the environment of the A ion during to tilting, (ii) the Sr atom is partially substituted by an atom (Ba) of higher ionic radios and (iii) the Jahn–Teller effect in by the partial removal of the e_g and t_{2g} degeneracies from cubic to tetragonal models. In previous studies, the same behavior has been observed by Joseph et al. [58].

Additionally, the structural study of the pristine BST_c and BST_t, $BSTS_c$, and $BSTS_t$ crystals was performed by X-ray diffraction (XRD) pattern using VESTA software. The XRD pattern for the BST_c, $BSTS_c$, BST_t, and $BSTS_t$ structures is shown in Fig. 2(a-d), and indicates a single-phase cubic and tetragonal perovskite with the *Pm-3 m* and *P4mm* space group, respectively.

The simulation of XRD patterns for the cubic BST and BSTS (Fig. 2a-b) is in good agreement with the crystallographic report JCPDS 39–1395, according to experimental data reported by Souza et al. [56]. In both crystals, the strongest peak around $2\theta = 32°$ corresponds to the (110) crystalline plane; however, doping with Sn^{4+} cations induces a shift of the main reflections toward 2θ values with the formation of clusters of $[SnO_6]$, from 32.11 to 31.42(°), due to the different electronic density to Ti^{4+} ions, which can be seen from the strongest diffraction peak

Table 1 Theoretical and Experimental lattice parameters, unit cell volume, and percentual error for BST_c, BST_t, $BSTS_c$, $BSTS_t$ materials

Sample BST	Cell volume[a] (Å)^3	$\alpha = \beta = \gamma = 90°$					
		Experimental		Theoretical		Percentual error (%)	
		$a = b = c$ (Å)		$a = b = c$ (Å)		$a = b = c$ (Å)	
BST_c	61.994	3.957		3.939		0.454	
$BSTS_c$	63.286	3.985		4.023		0.953	
		$a = b$ (Å)	c (Å)	$a = b$ (Å)	c (Å)	$a = b$ (Å)	c (Å)
BST_t	63.415	3.980	4.002	3.930	3.982	1.256	0.499
$BSTS_t$	63.731	3.991	4.000	4.022	4.012	0.776	0.300

[a]Experimental

Fig. 1 Conventional unit cell for pristine $(Ba,Sr)TiO_3$ and Sn-doped structures **a** cubic, **b** tetragonal polymorphs, **c** $[Ba,SrO_{12}]$, $[TiO_6]$ and $[SnO_4]$ clusters
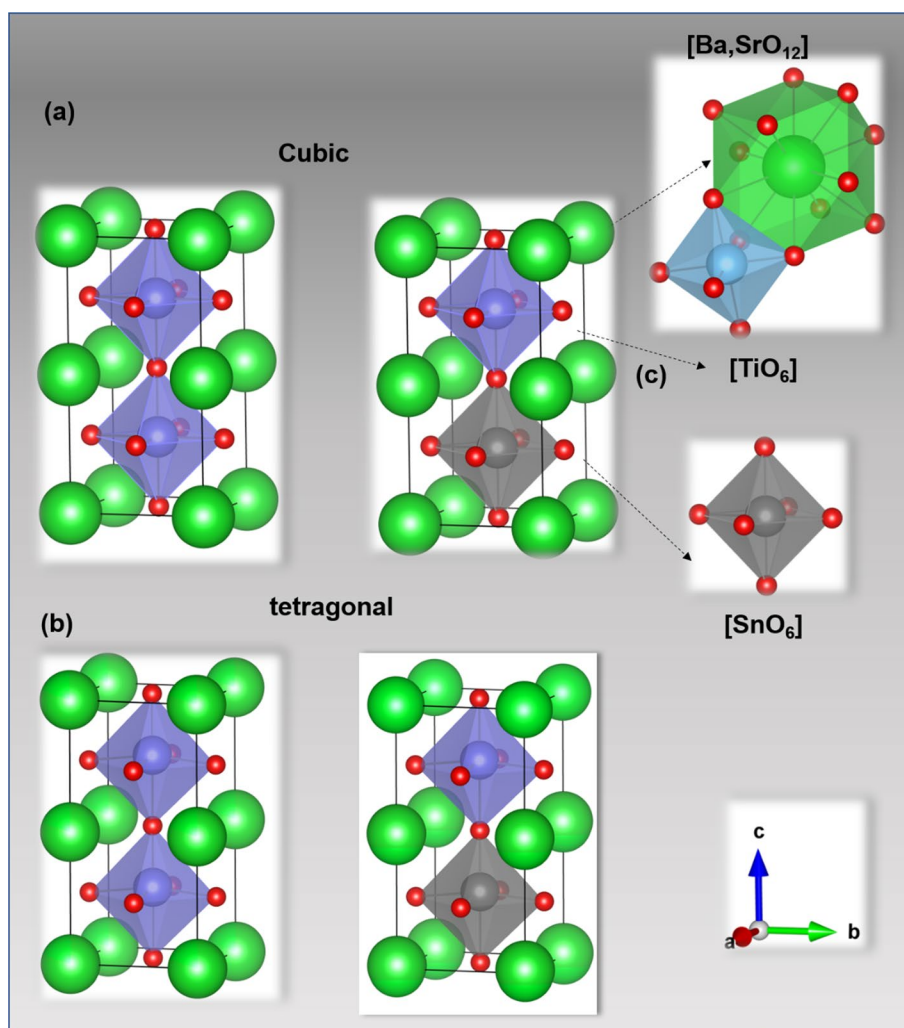

(Fig. 2a–b). The same was also observed for the following diffraction peaks changing from 39.60 to 38.87(°); 46.05 to 45.03(°), 57.24 to 55.96 (°), continuously for BST_c and $BSTS_c$. Moreover, in the doped system, some crystallographic planes were barely noticeable due to the low intensity as (100), (300), (212), (026), and (304). This observation is a strong indication of the successful substitution of Ti^{4+} by Sn^{4+} in the B sites of the perovskite BST_c material. Our observation for the simulation of XRD patterns of BST_t (Fig. 2c–d) follows the previous study reported by Chihaoui et al. [57]. The tetragonal phase and space group *P4mm* is confirmed by the presence of peaks (001), (100), (101), (110), (012), (111), (004), (200), (002), (102), (210), (211), (112), (220), (202), (204), (300), (212), (103), (310), (032), (106), (016), ((132), (312), (116), (224) and (133). In this case, similar behavior was observed for the doped system, as mentioned in the cubic system. In pristine BST_c and BST_t crystals structures, the main observation was the appearance of crystallographic plans, as shown in Fig. 2a and c.

3.2 Electronic properties

In this section, we present the theoretical results for the electronic properties of the investigated perovskite compounds. The electron distribution plays a fundamental role in determining the band structure, the density of states (DOS), and the charge density. The band structures plotted along the path Γ (0,0,0), X (½,0,0), M (½,½,0), Z (0,0, ½), R (½,0, ½), and A (½,½,½), as well as the calculated DOS projected for the atoms of the BST_c, BST_t, $BSTS_c$ and $BSTS_t$ crystals are displayed in Fig. 3a–b. These figures show that the shaded region in the band structure indicates the bandgap region, while pink bands indicate the valence band maximum (VBM) and conduction band minimum (CBM).

An analysis of the band structure and projected DOS are presented in Fig. 3a–b. For BST_c it was observed that the valence band (VB) is observed between 0 and − 4 eV. The conduction band (CB) was evaluated between 3.73 eV and 12 eV. The calculated indirect band gap energy was 3.73 eV, being an indirect electronic excitation between M
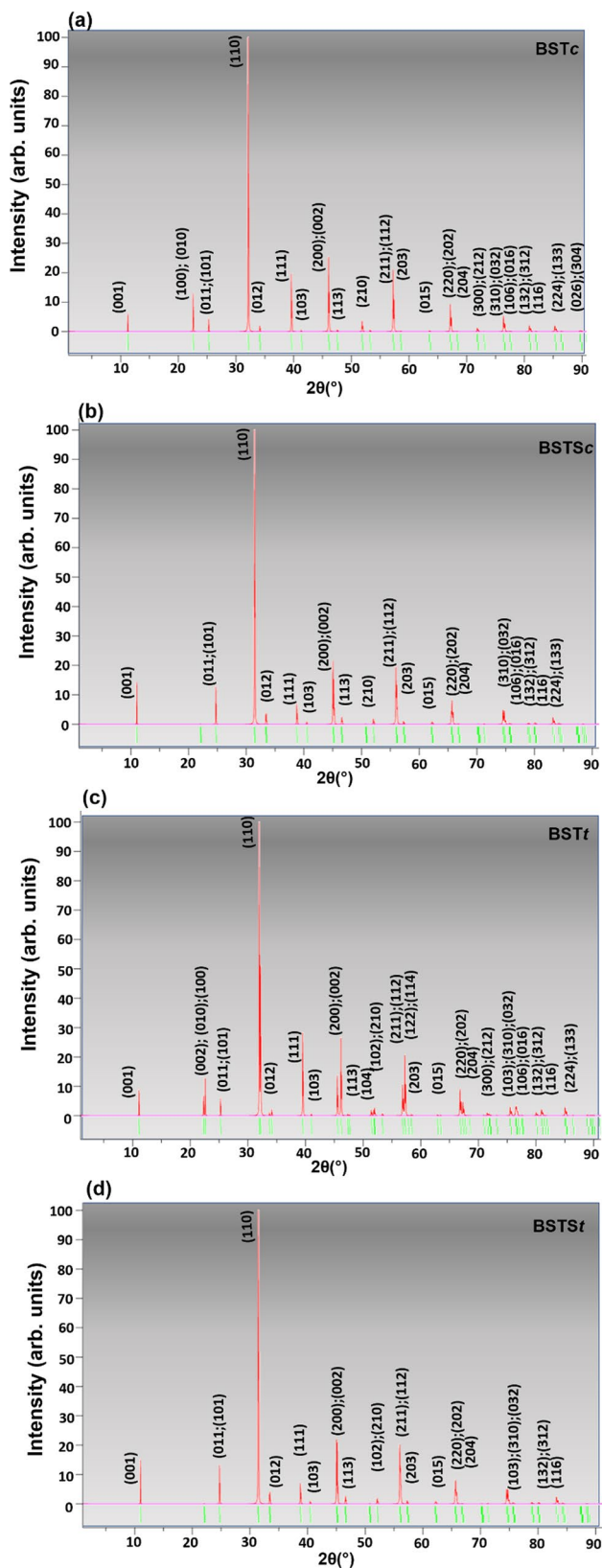
Fig. 2 Simulated X-ray diffraction patterns of **a** BST$_c$, **b** BSTS$_c$, **c** BST$_t$, and **d** BSTS$_t$ models by VESTA software

and Γ points. On the other hand, for the BST$_t$ structure the VB was taken between 0 and − 4 eV, while CB is between 3.76 and 12 eV. Regarding the bandgap region, an indirect electronic transition between M- Γ points was calculated around 3.76 eV. From BSTS$_c$ illustrated in Fig. 3, the VB was evaluated between 0 and − 4 eV. The CB is between 3.77 and 18 eV. For BSTS$_t$, the VB was evaluated between 0 and − 4 eV and CB is between 3.77 and 18 eV, where a bandgap energy of 3.77 eV was calculated between M-G.

The introduction of Sn^{4+} dopants causes slight changes in the bandgap energy (3.77 eV) of BSTS$_c$, originating from the intermediate electronic level due to the appearance of the localized states into the CB region from 4d Sn atomic orbitals. The dopant forms clusters that influence the short, medium and long range, the electronic density of the crystal, due to symmetry breaking. In this way, the results show the role of the dopant by introducing new properties to the semiconductor. This analysis is valid for the other dopants. Moreover, the detailed analysis of the upper panel of Fig. 3 indicates that Sn-doping mechanism affects the band distribution, mainly in the VB. Comparing the bands distribution for BST and BSTS models at different crystalline structures, it was noted that occupied electronic levels for BSTS are more degenerated in comparison with BST, which can be associated with the bonding character of Sn–O and Ti–O chemical bonds.

Besides, comparing the CB for both models of BST and BSTS enables us to interpret the charge carriers properties (electrons) from the curvature of Conduction Band Minimum (CBM). Indeed, for BST models the CBM located at G point is almost linear up to *X*, showing a broad feature, while the CBM for BSTS models at the same point exhibit a parabolic-like distribution with a well-located minimum point. Based on the relation between the effective mass of charge carriers with the band curvature, we can argue that electron–hole recombination rate is distinct between BST and BSTS models. In this case, a broader band can induce a higher effective mass for the excited electrons reducing its mobility, while a well-defined parabolic band can be associated with a reduced effective mass and higher electron mobility. Therefore, the obtained results for band structure profiles of BST and BSTS indicate that Sn-doping induces a higher electron mobility, making BSTS a good candidate for electro-optical applications.

As regard the obtained bandgap values, experimental and theoretical values were compared, as shown in Table 2, evidencing a good agreement. Indeed, the B3LYP hybrid functional showed a very close representation of the experimental bandgap energy, showing deviation ranging from 2.19 to 13.5%. Here, it is important to point out that bandgap description is a challenging topic for quantum mechanical calculations due to the treatment of exchange–correlation

(a)
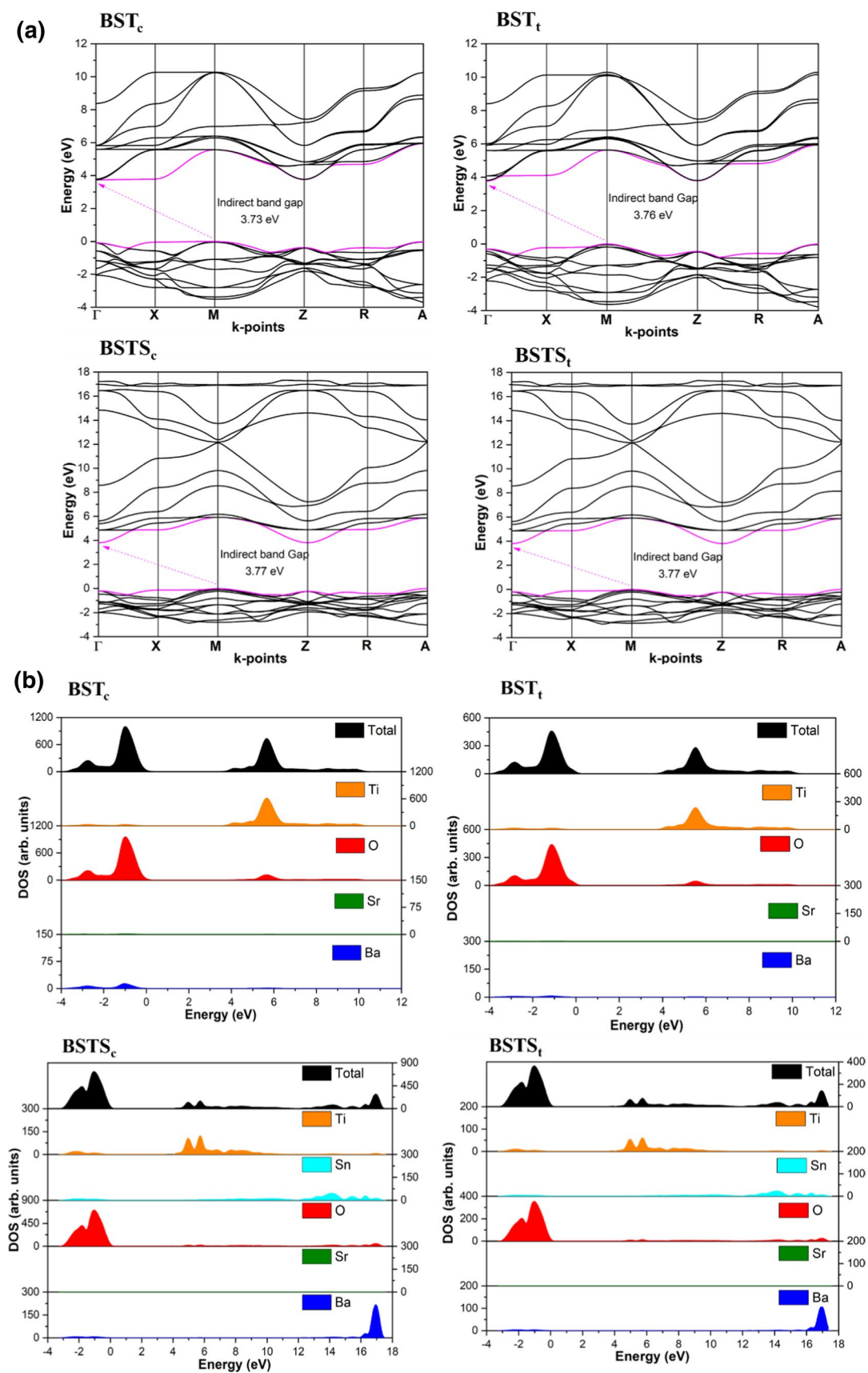
Fig. 3 **a** Band structure profiles and **b** atom-resolved DOS profiles for BST$_c$, BST$_t$, BSTS$_c$, and BSTS$_t$

effects. However, the obtained results confirm the predictive power of hybrid B3LYP functional for perovskite materials.

Additionally, Fig. 3b summarizes the analysis atomic contribution for both VB and CB, showing a well-defined pattern that is directly associated with the local clusters centered on Ba, Sr, Sn, Ti, and O atoms. The main contribution to the VB region is due to the 2p (px, py, pz) orbitals of the oxygen anions with a small content of Ba and Sr orbitals for both BST and BSTS models. In contrast, the CB was mostly based on empty valence ($3dxz$, $3dxy$, $3dyz$, $3dz^2$, $3dx^2\text{-}y^2$)

Table 2 Calculated and experimental values of the bandgap energy of BST_c, BST_t, $BSTS_c$, and $BSTS_t$

Perovskite compounds	Experimental (eV)	This work (eV)	Percentual error (%)
BSTc	3.65 [59]	3.73	2.19
BSTt	3.32 [59]	3.77	13.55
BSTSc	3.35 [60]	3.76	12.23
BSTSt	–	3.77	–

orbitals from Ti atom and a small content of Sn cations hybridized with oxygen atomic orbitals, revealing the role of [TiO_6] and [SnO_6] clusters. These results confirm the role of Sn-doping mechanism in the control of CBM distribution, which can be associated with the electron mobility along the electronic structure, as previously discussed.

Electronic density maps of the BST_c, BST_t, $BSTS_c$, and $BSTS_t$, were obtained from the optimized wavefunction, where the electronic density matrix was resolved as isolines that describe the density in an area, as an exhibit in Fig. 4(a-d). These electronic density maps were described along the Ba–O, Sr–O, Ti–O, and Sn–O bonds direction of the materials, which corresponds more specifically to the diagonal (110) plane for all models of cubic and tetragonal symmetries (Fig. 4a–d).

Figure 4(a–d) illustrates the strongly covalent character in the interaction of the Ti and Sn atoms with the oxygen atoms on the analyzed (110) plane, which is represented by homogenous distributions of the contour lines. The observed behavior takes place because of the hybridization between the oxygen 2p atomic orbitals and the Ti (3d) and Sn (4d)

Fig. 4 Electron density maps in the diagonal plane (110) for **a** BST_c, **b** $BSTS_c$, **c** BST_t and **d** $BSTS_t$ crystals structures
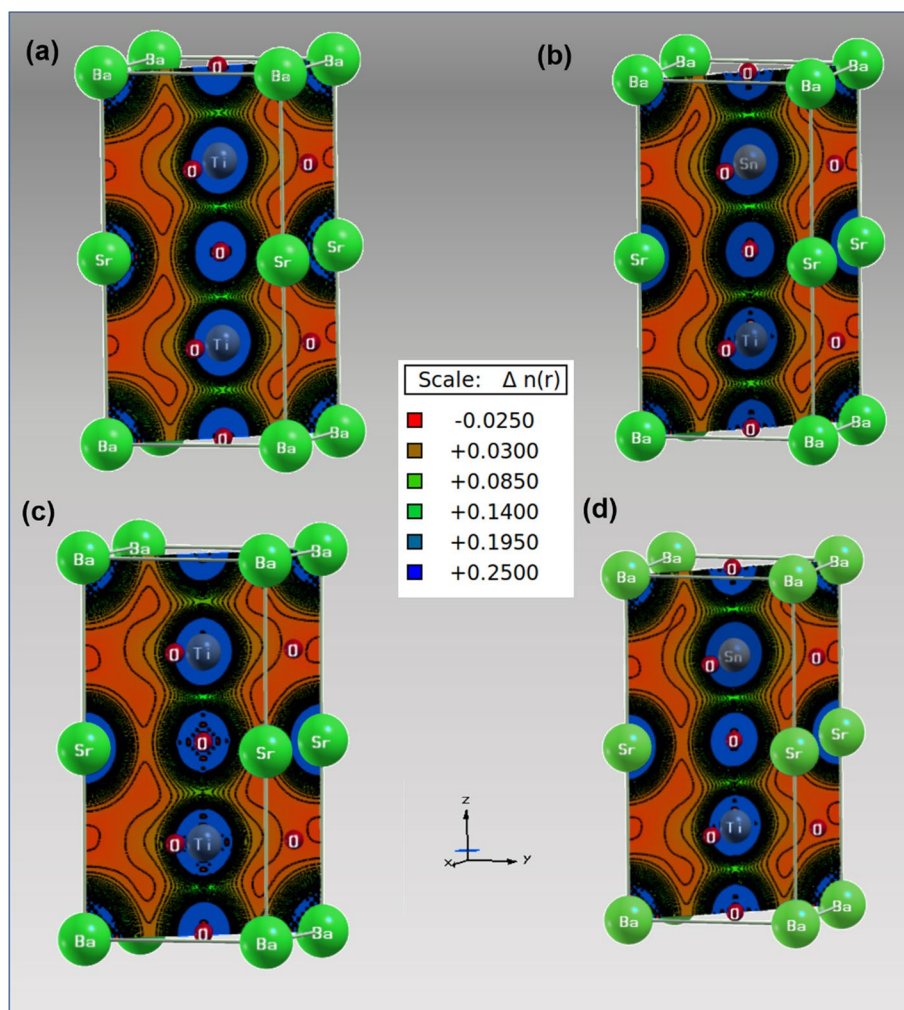
atomic orbitals. The density distribution remained the same for Fig. 4(a–c) illustrating the inhomogeneous distribution of the contour lines that represent the ionic character of the Ba–O and Sr–O bonds.

Furthermore, the significant difference between the contour plots reported in Fig. 4(a–d) is associated with the charge corridor along the z-axis for BST_c, BST_t, $BSTS_c$, and $BSTS_t$ models. In particular, for both cubic models (BST_c and $BSTS_c$), the charge corridor exhibits a homogenous distribution for electron density along the Ti–O–Ti or Sn–O–Ti bond path. On the other hand, for BST_t and $BSTS_t$, the intermetallic Ti–O–Ti showed a charge depletion area for a bridge-like oxygen atom, confirming the existence of spontaneous polarization along the [001] direction due to the off-centering atomic displacement for Ti atoms in tetragonal symmetry [3].

3.3 Vibrational properties

According to group theory, cubic perovskite with space group, O_h^1, *Pm-3 m* (221), has no Raman-active phonon modes. In contrast, tetragonal perovskite with space group, C_{4v}^1, *P4mm* (99) has the following phonon modes at the Γ point:

$$\Gamma_{\text{optical}} = 3A_1 + 4E + B_1$$

In the cubic phase (m-3 m), the zone-center optical phonons belong to $3F_{1u} + F_{2u}$ irreducible representations. Each of the F_u modes is triply degenerate, and all of them are of odd symmetry concerning the inversion, therefore, Raman inactive. The F_{1u} modes are infrared active, while the F_{2u} modes are silent. Upon transition to the tetragonal phase (4 mm), the F_{1u} modes split into A_1 and E modes, and the F_{2u} phonon gives rise to B_1 and E modes.

The A_1 and E modes are both Raman and infrared active, while the B_1 mode is only Raman active. The four optical E modes for the tetragonal phase are doubly degenerate and polarized along the x and y axes, and the three optical A_1 modes are polarized along the z-axis. The E and A_1 modes are split into longitudinal (LO) and transverse (TO) components as a result of long-range electrostatic forces associated with lattice ionicity [17, 61, 62]. Table 3 summarizes the experimental Raman active modes (cm^{-1}) for tetragonal or pseudo-cubic perovskite BST.

Thus, tetragonal BST has the Raman active crystal symmetry of C_{4v}^1, showing distinguishable Raman peaks at room temperature, in contrast to the cubic BST of the Raman inactive O_h^1 symmetry, for which the peaks disappear. This means that it is possible to discern crystal phases according to the Raman spectrum.
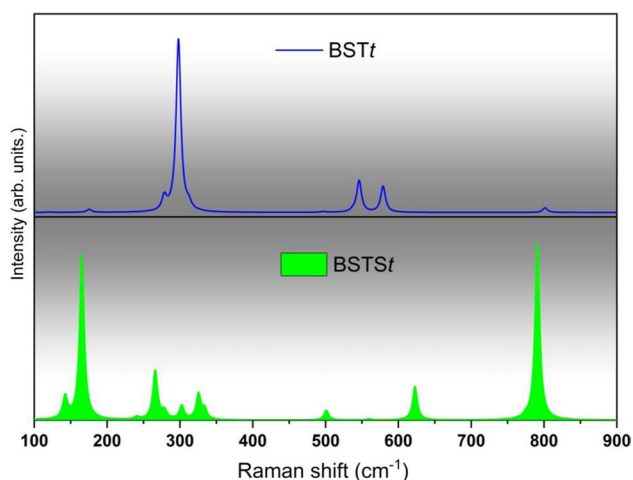
Figure 5 shows the calculated Raman spectra of the BST_t and $BSTS_t$ at the B3LYP level of theory in the frequency range 100–900 cm^{-1}. On the Raman spectrum of the tetragonal BST crystal structure, we observe seven active vibration modes observed at 121, 178, 280, 298, 546, 579, and 801 cm^{-1}. It is well known that DFT calculation at the B3LYP method tends to overestimate the values of the vibrational frequencies; therefore, a scaling factor of 0.94 is used [66].

Analyzing Fig. 5, it was observed that theoretical results are in good agreement with experimental data reported by Chihaoui et al. and other papers presented in Table 3. The bands around 180, 280 and 579 cm^{-1} are assigned to the transverse optical (TO) mode of A_1 symmetry, whereas the band around 298 and 801 cm^{-1}, which are characteristic of the tetragonal phase, are attributed to the E (TO + LO) + B_1 mode and A_1(LO) + E(LO) [34]. The A_1 longitudinal optic (LO) modes can be identified at 121 and 546 cm^{-1}. Nine peaks ascribed to the $BSTS_t$ Raman spectrum are observed at 100–900 cm^{-1} and seven for BST_t. This behavior means that the substitution for Sr and Sn in the A and B sites of the perovskite structure introduces a significant disorder in

Table 3 Experimental Raman active modes (cm^{-1}) for tetragonal or pseudo-cubic perovskite

Perovskite Compounds							
BST							
Modes							
A_1(LO$_1$)	A_1(TO$_1$)	A_1(TO$_2$)	B_1 and E(TO+LO)	A_1(LO$_2$) and E(LO)	E(TO) and A_1(TO$_3$)	A_1(LO$_3$) and E(LO)	Refs.
155	189	260	305	470	518	718	[63]
–	180	235	309	489	532	749	[57]
–	180	260	305	–	520	720	[61]
155	174	191	294	476	535	747	[62]
–	185	–	303	463	520	720	[17]
–	181	227	304	495	528	730	[64]
–	180	270	305	–	516	720	[65]

Fig. 5 Theoretical Raman spectra calculated for BST_t and $BSTS_t$ structures

Table 4 Calculated values of Formation Enthalpy (eV) before and after ZPE corrections for BST_c, BST_t, $BSTS_c$ and $BSTS_t$ perovskites, respectively

Models	ΔH_f	$\Delta H_f + ZPE$
BST_c	-2.610	-2.588
BST_t	-2.609	-2.573
$BSTS_c$	-2.157	-2.119
$BSTS_t$	-2.142	-2.101

the structure, favoring the relaxor character in the BSTS material.

3.4 Formation enthalpy and thermodynamic stability

The discussion involving the thermodynamic stability of perovskite polymorphs corresponds to an important topic due to the structural transformations associated with the symmetry order. In this context, the evaluation of Formation Enthalpy (ΔH_f) from its forming binary oxides plays a fundamental role in the discussion of phase stability [67–69]. From a theoretical point of view, such a process can be interpreted as a function of the reaction involving the perovskite material (ABO_3) and its component oxides ($AO + BO_2$). In this case, the ΔH_f can be calculated as the difference between the lattice energies, following the expression [70, 71]:

$$\Delta H_f = H_{ABO_3} - \sum_i^{metaloxides} H_i$$

where $H_i = E_T + pV$. Here, E_T is the total energy the solid at $P = 0$, and the corresponding equilibrium structures were obtained by optimizing all of the geometric parameters. Additionally, the zero-point energy contribution was estimated from vibrational analyses for comparative purposes.

Herein, the overall phase stability was calculated for BST_c, BST_t, $BSTS_c$ and $BSTS_t$ perovskites, respectively. Table 4 summarizes the obtained results for ΔH_f as a function of the component oxides (BaO, SrO, TiO_2 for BST_c and BST_t; BaO, SrO, TiO_2, SnO_2 for $BSTS_c$ and $BSTS_t$, respectively).

At first glance, it was observed that all investigated reaction channels indicate that BST_c, BST_t, $BSTS_c$ and $BSTS_t$

perovskites are stable in comparison with its component oxides, once negative values were founded. Moreover, the contribution of ZPE was calculated to be 0.022, 0.036, 0.038, and 0.041 eV for BST_c, BST_t, $BSTS_c$ and $BSTS_t$ perovskites, respectively. However, the stability order remains the same, even with the ZPE correction.

Further, comparing the ΔH_f for different polymorphs of BST (BST_c and BST_t), the calculated values indicate that the cubic phase is more stable in comparison with tetragonal symmetry. However, the values are quite similar, indicating the existence of a few differences between the crystalline structures. Similarly, the obtained values for tetragonal and cubic polymorphs of $BSTS_t$ indicate that the high-symmetric cubic lattice is more stable than tetragonal lattice, notwithstanding the polymorphs are very close in energy. Therefore, it was possible to observe that BST and BSTS perovskites are stable in comparison with their component oxides, being the cubic polymorph the low-energy arrangement expected in the complex phase diagram with the tetragonal phase.

3.5 Dielectric properties

Perovskite materials, such as BST, have been attracted an increased interest due to their inherent high dielectric constant [72–74]. In this context, the possibility to rationalize the dielectric properties through quantum–mechanical calculations correspond to an alternative tool to design new materials with potential technological applications. Herein, the static dielectric tensor (ε_0) was evaluated by means of Couple-perturbed Kohn–Sham scheme (CPKS) combined with longitudinal-transverse optical (LO-TO) splitting, [75–77] as reported in Table 5.

Our theoretical results for both BST_t and $BSTS_t$ materials show that both oxides were described by two independent components of the static dielectric (ε_0) tensor, where the ε_0^{zz} is the dominant. Moreover, our purpose is to investigate the dielectric behavior of $BSTS_t$ materials in order to compare with BST_t. Therefore, it was observed that for $BSTS_t$ the calculated values of the static dielectric tensor are smaller than for BST_t for the dominant ε_0^{zz} component. On the other hand, the ε_0^{xx} component for BST_t becomes higher than for $BSTS_t$. This effect may be related to a higher mobility of Sn atom, which induces a greater asymmetry in the electronic density of BO_6 octahedral reducing the dielectric constant. In particular, the obtained results

Table 5 Independent components of static dielectric tensor (ε_0) for BST$_t$ and BSTS$_t$ perovskites, respectively

Models	ε_0^{xx}	ε_0^{zz}
BST$_t$	2.053	22.654
BSTS$_t$	5.697	17.850

confirms the superior dielectric behavior of BST$_t$, but also shed a light on BSTS$_t$ perovskite materials as promising candidates for dielectric devices.

4 Conclusion

In summary, pristine cubic and tetragonal BST (BSTc and BSTt) and Sn-doped BST (BSTSc and BSTSt) were investigated from the Density Functional Theory calculations to gain an in-depth understanding of structural, electronic, vibrational and energetic properties. XRD patterns by VESTA software and DFT analysis confirmed the perovskite phases showing both *Pm-3 m* and *P4mm* space groups in pristine and Sn-doped BST structures. The building blocks of the BSTc, BSTt, BSTSc, and BSTSt crystals, i.e., a local coordination structure for both the Ba, Sr, Ti, and Sn atoms, were confirmed as deltahedral [Ba,SrO$_{12}$], and octahedral [TiO$_6$], and [SnO$_6$] clusters. In the viewpoint of thermodynamic analysis, all models were calculated to be stable in comparison with their component oxides. The indirect bandgap energy was calculated as 3.73, 3.76, 3.77, and 3.77 eV for BSTc, BSTt, BSTSc, and BSTSt structures, respectively. Moreover, the detailed analysis of electronic structures for BST and BSTS models indicates that Sn-doping induces a higher electron mobility, being a potential candidate for electro-optical applications. Such results indicate that the change in geometry and insertion of the Sn atom generates an intrinsically order–disorder effect, which will promote a presence of intermediate levels, causing an increase in the gap energy. According to the charge density maps, the periodic models showed well-defined electron density distribution characterizing the symmetrical structure and confirmed the covalent bonds between transition Ti and Sn metals with oxygen atoms, while the Sr–O and Ba–O bonds were defined as ionic. Moreover, the vibrational analysis indicates the presence of singular disorders for BSTt and BSTSt associated with the doping process along with the A- and B-site of perovskite structure, resulting in a more pronounced relaxor character for BSTSt. For the dielectric applications, it was observed that dielectric tensor components for BSTSt were comparable with the calculated values for BSTt, suggesting a potential application in dielectric devices. These results were an essential tool for understanding the electronic and structural effects caused by a change in geometry and element doping on the perovskite BST structure.

References

1. Mohamed EA, Nabhan E, Ratep A, Hassan FM, Tahoon K (2020) Influence of BaTiO$_3$ nanoparticles/clusters on the structural and dielectric properties of glasses-nanocomposites. Phys B Condens Matter 589:412220
2. Stanciu CA, Cernea M, Secu EC, Aldica G, Ganea P, Trusca R (2017) Lanthanum influence on the structure, dielectric properties and luminescence of BaTiO$_3$ ceramics processed by spark plasma sintering technique. J Alloys Compd 706:538–545
3. Piskunov S, Eglitis RI (2015) First principles hybrid DFT calculations of BaTiO$_3$/SrTiO$_3$ (001) interface. Solid State Ion 274:29–33
4. Chao S, Dogan F (2011) BaTiO$_3$–SrTiO$_3$ layered dielectrics for energy storage. Mater Lett 65(6):978–981
5. Kang F, Zhang L, Huang B, Mao P, Wang Z, Sun Q, Wang J, Hu D (2020) Enhanced electromechanical properties of SrTiO$_3$-BiFeO$_3$-BaTiO$_3$ ceramics via relaxor behavior and phase boundary design. J Eur Ceram Soc 40(4):1198–1204
6. Jongprateep O, Sato N (2019) Effects of sintering temperatures on microstructure and dielectric constant of Ba$_{0.05}$Sr$_x$Ca$_{0.95-x}$TiO$_3$ where (x = 0, 0.475 and 0.95). Mater Today-Proc 17:1898–1905
7. Fujisawa J-i, Eda T, Hanaya M (2017) Comparative study of conduction-band and valence-band edges of TiO$_2$, SrTiO$_3$, and BaTiO$_3$ by ionization potential measurements. Chem Phys Lett 685:23–26
8. Gartnerova V, Pacherova O, Klinger M, Jelinek M, Jager A, Tyunina M (2017) Strain fluctuations in BaTiO$_3$/SrTiO$_3$ heterostructures. Mater Res Bull 89:180–184
9. Mbarki R, Haskins JB, Kinaci A, Cagin T (2014) Temperature dependence of flexoelectricity in BaTiO$_3$ and SrTiO$_3$ perovskite nanostructures. Phys Lett A 378(30):2181–2183
10. Assirey EAR (2019) Perovskite synthesis, properties and their related biochemical and industrial application. Saudi Pharm J 27(6):817–829
11. Kondo S, Yamada T, Tagantsev AK, Ma P, Leuthold J, Martelli P, Boffi P, Martinelli M, Yoshino M, Nagasaki T (2019) Large impact of strain on the electro-optic effect in (Ba, Sr)TiO$_3$ thin films: experiment and theoretical comparison. Appl Phys Lett 115(9):092901
12. Gao L, Guan Z, Huang S, Liang K, Chen H, Zhang J (2019) Enhanced dielectric properties of barium strontium titanate thin films by doping modification. J Mater Sci Mater Electron 30(14):12821–12839

13. Xing Y, Liang H, Li X, Si L (2009) High-frequency dielectric properties of BSTO ceramic prepared with hydrothermal synthesized $SrTiO_3$ and $BaTiO_3$ powders. Particuology 7(5):414–418

14. Slimani Y, Unal B, Hannachi E, Selmi A, Almessiere MA, Nawaz M, Baykal A, Ercan I, Yildiz M (2019) Frequency and dc bias voltage dependent dielectric properties and electrical conductivity of $BaTiO_3SrTiO_3/(SiO_2)_x$ nanocomposites. Ceram Int 45(9):11989–12000

15. Kim SW, Choi HI, Lee MH, Park JS, Kim DJ, Do D, Kim MH, Song TK, Kim WJ (2013) Electrical properties and phase of $BaTiO_3$–$SrTiO_3$ solid solution. Ceram Int 39:S487–S490

16. Yustanti E, Hafizah MAE, Manaf A (2016) Synthesis of strontium substituted barium titanate nanoparticles by mechanical alloying and high power ultrasonication destruction. AIP Conf Proc 1725(1):020102

17. Pasha UM, Zheng H, Thakur OP, Feteira A, Whittle KR, Sinclair DC, Reaney IM (2007) In situ Raman spectroscopy of A-site doped barium titanate. Appl Phys Lett 91(6):062908

18. Berbecaru C, Alexandru HV, Porosnicu C, Velea A, Ioachim A, Nedelcu L, Toacsan M (2008) Ceramic materials $Ba_{(1-x)}Sr_xTiO_3$ for electronics—synthesis and characterization. Thin Solid Films 516(22):8210–8214

19. Mohan CRK, Bajpai PK (2008) Effect of sintering optimization on the electrical properties of bulk $Ba_xSr_{1-x}TiO_3$ ceramics. Phys B Condens Matter 403(13):2173–2188

20. Shen Z-Y, Wang Y, Tang Y, Yu Y, Luo W-Q, Wang X, Li Y, Wang Z, Song F (2019) Glass modified barium strontium titanate ceramics for energy storage capacitor at elevated temperatures. J Materiomics 5(4):641–648

21. Hou B, Xu Y, Wu D, Sun Y (2006) Preparation and characterization of single-crystalline barium strontium titanate nanocubes via solvothermal method. Powder Technol 170(1):26–30

22. Irzaman PIR, Aminullah SH, Alatas H (2016) Development of ferroelectric solar cells of barium strontium titanate ($Ba_xSr_{1-x}TiO_3$) for substituting conventional battery in LAPAN-IPB satellite (LISAT). Proc Environ Sci 33:607–614

23. Curecheriu LP, Mitoseriu L, Ianculescu A (2009) Nonlinear dielectric properties of $Ba_{1-x}Sr_xTiO_3$ ceramics. J Alloys Compd 482(1):1–4

24. Zuo XH, Deng XY, Chen Y, Ruan M, Li W, Liu B, Qu Y, Xu B (2010) A novel method for preparation of barium strontium titanate nanopowders. Mater Lett 64(10):1150–1153

25. Jung DS, Hong SK, Cho JS, Kang YC (2008) Morphologies and crystal structures of nano-sized $Ba_{1-x}Sr_xTiO_3$ primary particles prepared by flame spray pyrolysis. Mater Res Bull 43(7):1789–1799

26. Rashad MM, Turky AO, Kandil AT (2013) Optical and electrical properties of $Ba_{1-x}Sr_xTiO_3$ nanopowders at different Sr^{2+} ion content. J Mater Sci Mater Electron 24(9):3284–3291

27. Simões AZ, Moura F, Onofre TB, Ramirez MA, Varela JA, Longo E (2010) Microwave-hydrothermal synthesis of barium strontium titanate nanoparticles. J Alloys Compd 508(2):620–624

28. Alexandru HV, Berbecaru C, Ioachim A, Nedelcu L, Dutu A (2006) BST solid solutions, temperature evolution of the ferroelectric transitions. Appl Surf Sci 253(1):354–357

29. Veselinović L, Mitrić M, Mančić L, Vukomanović M, Hadžić B, Marković S, Uskoković D (2014) The effect of Sn for Ti substitution on the average and local crystal structure of $BaTi_{1-x}Sn_xO_3$ ($0 \leq x \leq 0.20$). J Appl Crystallogr 47(3):999–1007

30. Watanabe Y (2019) Accurate semiempirical analytical formulas for spontaneous polarization by crystallographic parameters of $SrTiO_3$-$BaTiO_3$ system by ab initio calculations. Comput Mater Sci 158:315–323

31. Atta NF, Ahmed Galal, El-Ads EH (2016) Perovskite nanomaterials—synthesis, characterization, and applications. In: Likun P, Zhu G (eds) Perovskite materials—synthesis, characterisation, properties, and applications. IntechOpen

32. Piskunov S, Eglitis RI (2016) Comparative ab initio calculations of $SrTiO_3/BaTiO_3$ and $SrZrO_3/PbZrO_3$ (001) heterostructures. Nucl Instrum Methods Phys Res B 374:20–23

33. Lee H-S, Mizoguchi T, Yamamoto T, Kang S-JL, Ikuhara Y (2007) First-principles calculation of defect energetics in cubic-$BaTiO_3$ and a comparison with $SrTiO_3$. Acta Mater 55(19):6535–6540

34. Zhang R-z, Hu X-y, Guo P, Wang C-l (2012) Thermoelectric transport coefficients of n-doped $CaTiO_3$, $SrTiO_3$ and $BaTiO_3$: a theoretical study. Phys B Condens Matter 407(7):1114–1118

35. Rizwan M, Hajra ZI, Shakil M, Gillani SSA, Usman Z (2020) Electronic, structural and optical properties of $BaTiO_3$ doped with lanthanum (La): insight from DFT calculation. Optik 211:164611

36. Dovesi R, Orlando R, Erba A, Zicovich-Wilson CM, Civalleri B, Casassa S, Maschio L, Ferrabone M, De La Pierre M, D'Arco P, Noël Y, Causà M, Rérat M, Kirtman B (2014) CRYSTAL14: a program for the ab initio investigation of crystalline solids. Int J Quantum Chem 114(19):1287–1317

37. Lee CT, Yang WT, Parr RG (1988) Development of the Colle-Salvetti correlation-energy formula into a functional of the electron density. Phys Rev B Condens Matter 37:785–789

38. Becke AD (1993) Density-functional thermochemistry. III. The role of exact exchange. J Chem Phys 98:5648–5652

39. Longo VM, Cavalcante LS, Erlo R, Mastelaro VR, de Figueiredo AT, Sambrano JR, de Lázaro S, Freitas AZ, Gomes L, Vieira ND, Varela JA, Longo E (2008) Strong violet–blue light photoluminescence emission at room temperature in $SrZrO_3$: joint experimental and theoretical study. Acta Mater 56(10):2191–2202

40. Longo VM, Figueiredo ATd, Lázaro Sd, Gurgel MF, Costa MGS, Paiva-Santos CO, Varela JA, Longo E, Mastelaro VR, Vicente FSD, Hernandes AC, Franco RWA (2008) Structural conditions that leads to photoluminescence emission in $SrTiO_3$: an experimental and theoretical approach. J Appl Phys 104(2):023515

41. Longo VM, Cavalcante LS, Costa MGS, Moreira ML, de Figueiredo AT, Andrés J, Varela JA, Longo E (2009) First principles calculations on the origin of violet-blue and green light photoluminescence emission in $SrZrO_3$ and $SrTiO_3$ perovskites. Theor Chem Acc 124(5):385

42. Moreira E, Henriques JM, Azevedo DL, Caetano EWS, Freire VN, Albuquerque EL (2011) Structural, optoelectronic, infrared and Raman spectra of orthorhombic $SrSnO_3$ from DFT calculations. J Solid State Chem 184(4):921–928

43. Oliveira MC, Gracia L, de Assis M, Rosa ILV, do Carmo Gurgel MF, Longo E, Andrés J (2017) Mechanism of photoluminescence in intrinsically disordered $CaZrO_3$ crystals: first principles modeling of the excited electronic states. J Alloys Compd 722:981–995

44. Oliveira MC, Ribeiro RAP, Gracia L, de Lazaro SR, de Assis M, Oliva M, Rosa ILV, Gurgel MFdC, Longo E, Andrés J (2018) Experimental and theoretical study of the energetic, morphological, and photoluminescence properties of $CaZrO_3$:Eu^{3+}. CrystEngComm 20(37):5519

45. Tranquilin RL, Lovisa LX, Almeida CRR, Paskocimas CA, Li MS, Oliveira MC, Gracia L, Andres J, Longo E, Motta FV, Bomio MRD (2019) Understanding the white-emitting $CaMoO_4$ Co-Doped Eu^{3+}, Tb^{3+}, and Tm^{3+} phosphor through experiment and computation. J Phys Chem C 123(30):18536–18550

46. Oliveira MC, Andrés J, Gracia L, de Oliveira MSMP, Mercury JMR, Longo E, Nogueira IC (2019) Geometry, electronic structure, morphology, and photoluminescence emissions of $BaW_{1-x}Mo_xO_4$ (x = 0, 0.25, 0.50, 0.75, and 1) solid solutions: theory and experiment in concert. Appl Surf Sci 463:907–917

47. Eglitis R, Kruchinin SP (2020) Ab initio calculations of ABO_3perovskite (001), (011) and (111) nano-surfaces, interfaces and defects. Mod Phys Lett B 34(19n20):2040057

48. Eglitis RI (2019) Ab initio calculations of $CaZrO_3$, $BaZrO_3$, $PbTiO_3$ and $SrTiO_3$ (001), (011) and (111) surfaces as well as their (001) interfaces. Integr Ferroelectr 196(1):7–15

49. Eglitis R, Purans J, Popov AI, Jia R (2019) Systematic trends in $YAlO_3$, $SrTiO_3$, $BaTiO_3$, $BaZrO_3$ (001) and (111) surface ab initio calculations. Int J Mod Phys B 33(32):1950390

50. Maul J, Santos IMG, Sambrano JR, Erba A (2016) Thermal properties of the orthorhombic $CaSnO_3$ perovskite under pressure from ab initio quasi-harmonic calculations. Theor Chem Acc 135(2):36

51. Cavalcante LS, Batista NC, Badapanda T, Costa MGS, Li MS, Avansi W, Mastelaro VR, Longo E, Espinosa JWM, Gurgel MFC (2013) Local electronic structure, optical bandgap and photoluminescence (PL) properties of $Ba(Zr_{0.75}Ti_{0.25})O3$ powders. Mat Sci Semicon Proc 16(3):1035–1045

52. Momma K, Izumi F (2011) VESTA 3 for three-dimensional visualization of crystal, volumetric and morphology data. J Appl Crystallogr 44(6):1272–1276

53. Kokalj A (1999) XCrySDen-a new program for displaying crystalline structures and electron densities. J Mol Graph Model 17(3–4):176–216

54. Monkhorst HJ, Pack JD (1976) Special points for Brillouin-zone integrations. Phys Rev B 13(12):5188

55. Shannon R (1976) Revised effective ionic radii and systematic studies of interatomic distances in halides and chalcogenides. Acta Cryst Sec A 32(5):751–767

56. Souza IA, Cavalcante LS, Sczancoski JC, Moura F, Paiva-Santos CO, Varela JA, Simões AZ, Longo E (2009) Structural and dielectric properties of $Ba_{0.5}Sr_{0.5}(SnxTi_{1−x})O_3$ ceramics obtained by the soft chemical method. J Alloys Compd 477(1):877–882

57. Chihaoui S, Seveyrat L, Perrin V, Kallel I, Lebrun L, Khemakhem H (2017) Structural evolution and electrical characteristics of Sn-doped $Ba_{0.8}Sr_{0.2}TiO_3$ ceramics. Ceram Int 43(1, Part A):427–432

58. Joseph J, Vimala TM, Raju J, Murthy VRK (1999) Structural investigations on the (Ba, Sr)(Zr, Ti)O_3 system. J Phys D Appl Phys 32(9):1049–1057

59. Turky AO, Rashad MM, Bechelany M (2016) Tailoring optical and dielectric properties of $Ba_{0.5}Sr_{0.5}TiO_3$ powders synthesized using citrate precursor route. Mater Des 90:54–59

60. Souza IA, Simões AZ, Longo E, Varela JA, Pizani PS (2006) Photoluminescence at room temperature in disordered $Ba_{0.50}Sr_{0.50}(Ti_{0.80}Sn_{0.20})O_3$ thin films. Appl Phys Lett 88(21):211911

61. Kuo S-Y, Liao W-Y, Hsieh W-F (2001) Structural ordering transition and repulsion of the giant LO-TO splitting in polycrystalline $Ba_xSr_{1−x}TiO_3$. Phys Rev B 64(22):224103

62. Tenne DA, Soukiassian A, Xi XX, Choosuwan H, Guo R, Bhalla AS (2004) Lattice dynamics in $Ba_xSr_{1−x}TiO_3$ single crystals: a Raman study. Phys Rev B 70(17):174302

63. Souza IA, Gurgel MFC, Santos LPS, Góes MS, Cava S, Cilense M, Rosa ILV, Paiva-Santos CO, Longo E (2006) Theoretical and experimental study of disordered $Ba_{0.45}Sr_{0.55}TiO_3$ photoluminescence at room temperature. Chem Phys 322(3):343–348

64. Ganjir R, Bajpai PK (2019) Influence of Co doping on the structural, dielectric and Raman properties of $Ba_{0.75}Sr_{0.25}Ti_1−xCoxO_3$. J Electron Mater 48(1):634–641

65. Bajpai PK, Mohan CRK, Ganjir R, Kumar R, Kumar A, Katiyar RS (2018) Swift heavy ion induced material modifications in $Ba_{1−x}Sr_xTiO_3$ ceramics as probed by temperature-dependent Raman spectroscopy. J Raman Spectrosc 49(2):324–335

66. Foresman J, Frisch A (2015) Exploring chemistry with electronic structure methods, 3rd edn. Gaussian Inc, Pittsburgh

67. Hautier G, Ong SP, Jain A, Moore CJ, Ceder G (2012) Accuracy of density functional theory in predicting formation energies of ternary oxides from binary oxides and its implication on phase stability. Phys Rev B 85(15):155208

68. Emery AA, Wolverton C (2017) High-throughput DFT calculations of formation energy, stability and oxygen vacancy formation energy of ABO_3 perovskites. Sci Data 4(1):170153

69. Kojitani H, Navrotsky A, Akaogi M (2001) Calorimetric study of perovskite solid solutions in the $CaSiO_3$–$CaGeO_3$ system. Phys Chem Miner 28(6):413–420

70. Beltrán A, Gracia L, Andrés J (2019) Polymorphs of ZnV_2O_6 under pressure: a first-principle investigation. J Phys Chem C 123(5):3239–3253

71. Beltrán A, Gracia L, Andrés J, Longo E (2017) First-principles study on polymorphs of $AgVO_3$: assessing to structural stabilities and pressure-induced transitions. J Phys Chem C 121(49):27624–27642

72. Nagaraj B, Sawhney T, Perusse S, Aggarwal S, Ramesh R, Kaushik VS, Zafar S, Jones RE, Lee JH, Balu V, Lee J (1999) (Ba, Sr)TiO_3 thin films with conducting perovskite electrodes for dynamic random access memory applications. Appl Phys Lett 74(21):3194–3196

73. Kuroiwa T, Tsunemine Y, Horikawa T, Makita T, Tanimura J, Mikami N, Sato K (1994) Dielectric properties of (Ba_xSr_{1-x}) TiO_3 thin films prepared by RF sputtering for dynamic random access memory application. Jpn. J Appl Phys 33(Part 1, No. 9B):5187–5191

74. Serraiocco J, Acikel B, Hansen P, Taylor T, Xu H, Speck JS, York RA (2002) Tunable passive integrated circuits using BST thin films. Integr Ferroelectr 49(1):161–170

75. Ferrero M, Rérat M, Orlando R, Dovesi R (2008) The calculation of static polarizabilities of 1–3D periodic compounds the implementation in the crystal code. J Comput Chem 29(9):1450–1459

76. Ferrero M, Rérat M, Orlando R, Dovesi R (2008) Coupled perturbed Hartree-Fock for periodic systems: the role of symmetry and related computational aspects. J Chem Phys 128(1):014110

77. Ferrero M, Rérat M, Kirtman B, Dovesi R (2008) Calculation of first and second static hyperpolarizabilities of one- to three-dimensional periodic compounds. Implementation in the CRYSTAL code. J Chem Phys 129(24):244110